Experiments in Fluids (2025) 66:141
https://doi.org/10.1007/s00348-025-04067-0

RESEARCH ARTICLE

Escaping the lab: advances in large-scale particle tracking using natural light and uncrewed aerial vehicles

Robin Leister[1] · David E. Rival[2]

Received: 20 December 2024 / Revised: 1 June 2025 / Accepted: 2 June 2025

Abstract

Here we explore the potential of the glare-point particle tracking (GPPT) technique for realistic field-scale measurements. We make use of a commercially available, drone-based camera to extract three-dimensional information under natural light conditions. Air-filled soap bubbles on the order of centimeters are used as seeding tracers. In the current tests, the suitability of the portable setup has been demonstrated for volumes up to 163 m^3. The frame-to-frame camera movement, caused by slight adjustments of the drone flying outdoors, could be quantified and corrected via an image-based approach. Both limits introduced through the larger tracer size and uncertainty caused by the glare-point approach are discussed accordingly. Furthermore, based on the fixed magnification of the drone camera, the limit in drone operation can be determined when the two most dominant, bubble-based glare points collapse onto one, which was observed well above a height of 10m. Finally, a turbulent free jet, exiting from a square-shaped nozzle with edge length 0.3 m, served as an exemplary test case. Tracks emerging at the jet exit all the way to 10 m downstream of the nozzle were successfully reconstructed in three dimensions. Lagrangian properties, such as flow acceleration, as well as pathline curvature at the integral length scale, were resolved in the large turbulent jet. This sparse yet accurate Lagrangian data over a large physical volume demonstrates insights into turbulent mixing processes at the integral length well beyond current Eulerian-based descriptions.

1 Introduction

Capturing the dynamics of large-scale atmospheric flows in both urban and rural settings is of importance for a variety of research disciplines, ranging from classical engineering applications around bluff bodies (e.g., wind turbines, photovoltaic plants, road vehicles, buildings) all the way through to local geophysical (microscale) flows, where insight into three-dimensional flow structures may lead to the improvement of current weather and climate models Bou-Zeid et al. (2020). Large-scale, three-dimensional particle tracking of said flow structures is, despite many advances in tracer, camera and processing technology, still an ambitious undertaking (Caridi et al. 2016; Wei et al. 2021; Kaiser and Rival 2023), mainly limited by the lack of scattered light from tracers and the need for cost-intensive equipment and setup using multiple high-speed cameras.

For the case of optical flow measurements in air, the most common tracers used at small scales are aerosol-based particles, e.g., di-ethyl-hexyl-sebacate (DEHS) or water–glycol particles, as nicely summarized in Raffel et al. (2018). The typical diameter of such droplets are in the range of $0.3 - 0.4$ µm (Fuchs et al. 2023). Such tiny seeding diameters are ideally suited for small-scale volumetric measurements on the order of $10^{-1} - 10^{2}$ cm^3 Barros et al. (2021), i.e., capturing a broad range turbulent scales and often applied due to their excellent flow-following behavior. As a source of illumination, most often lasers and pulsed LEDs are applied, and thus, the particle image that is visible on the camera sensor is therefore described via diffraction-limited imaging.

The limitations of a small measurement volume, due to a finite light scatter intensity, were partially resolved by introducing larger tracers (Bosbach et al. 2008). Helium-filled soap bubbles (HFSB) have a significant larger diameter in the range of $0.1 - 10$ mm (Grille Guerra et al. 2024; Conlin et al. 2024) and are—thanks to filling them with helium—neutrally buoyant despite their large size. The

✉ Robin Leister
robin.leister@kit.edu

[1] Institute of Fluid Mechanics (ISTM), Karlsruhe Institute of Technology (KIT), Kaiserstr. 10, 76131 Karlsruhe, Germany

[2] Institute of Fluid Mechanics (ISM), Technische Universität Braunschweig, Hermann-Blenk-Str. 37, 38108 Braunschweig, Germany

Published online: 28 June 2025

light scattering intensity is increased by four to five orders of magnitude when compared to aerosol-based tracers (Scarano et al. 2015). The flow-following behavior relative to the surrounding air flow, however, is reduced due to their inertial mass and diameter, lacking the possibility to resolve the finest scales of the turbulent motion (Faleiros et al. 2018). As one recent example, Schröder et al. (2022) illuminated a volume of 12 m^3 using HFSBs and six high-speed cameras.

If one is interested in capturing the Lagrangian statistics in even larger volumes, such as those found in atmospheric flows pertinent to micrometeorology, several solutions have been reported in the literature. Generally, an image-based measurement with yet even larger tracers will provide an acceptable flow-following behavior so long as the focus is on the large-scale, energy-containing structures, i.e., one must see this problem through the lens of low-pass filtering. Rosi et al. (2014) used air-filled soap bubbles with a diameter of 25mm, whereas Wei et al. (2021) used artificial snow and Bristow et al. (2023a) and Li et al. (2024) used natural snow as tracer particles. More recently, Conlin et al. (2024) used 8mm air-filled bubbles and nine 500W LED arrays for the characterization of the atmospheric surface layer within field-relevant scales. These approaches, however, require static multi-camera setups for the purpose of three-dimensional reconstruction. In contrast, Hou et al. (2021) and Kaiser and Rival (2023) describe a glare-point technique for large-scale volumetric particle tracking using a combination of air-filled soap bubbles (AFSBs) as tracers paired with the use of a single camera for a three-component three-dimensional (3D3C) reconstruction. The key differentiation in these latter studies lies in the so-called glare-point particle tracking (GPPT) technique where the estimation of the third spatial component of position (depth) is recovered via glare-point spacings from each of the AFSBs.

Recent developments in camera technology such as the back-illuminated sensor or the trend toward 4k video over the past few years have led to the availability of commercially available drones with onboard cameras. These onboard cameras include a number of advanced technical features such as the availability of higher frame rates, color video with more than 8 bits per channel and a considerably high image resolution. For instance, the current trend toward 4k video could only be found on high-end cameras just a few years ago. However, when applied to a scientific setup, these cameras lack some important features, like a global image shutter as well as a precise trigger, among other limitations. As an additional hurdle, the positional stabilization is a closed-source process, so no direct access is possible. For low-altitude levels, commercial quadcopters usually rely on visual–inertial odometry and barometric pressure sensors, which comes as a challenge for a precise scientific measurement. Nevertheless, over the last years, several companies have since introduced commercial-grade camera drones, with remarkable improvements in imaging and stabilization techniques.

Uncrewed aerial vehicles (UAVs) have been in place ever since the first image-based velocimetry approaches found their way into the fluid mechanics research community. Examples include Fujita and Hino (2003) or Detert and Weitbrecht (2014), where helicopters equipped with a camera were used to extract velocity information over a flowing river in a non-intrusive manner. Tracers including wooden debris or foam chips were used to extract flow features. The use of off-the-shelf, rotary-wing drones, i.e., UAVs, as opposed to helicopters, for 2D PIV evaluation have been performed by, e.g., Detert and Weitbrecht (2015) and Detert et al. (2019). In these studies, a 1.6×1.6 m^2 interrogation area, paired with seeding particles in the range of $30 - 40$ mm, was used for the extraction of the surface velocity on a river near a hydropower plant. A more recent example, was conducted by Bristow et al. (2023b), where onboard 2D PIV helped to measure smoke plumes with UAV-based imaging.

The current investigation couples the glare-point particle tracking (GPPT) approach, as first introduced by Hou et al. (2021), to a consumer-grade drone camera. Ultimately a drone-based imaging system provides access to field-relevant scales in a time- and cost-effective manner. The sun is used for natural illumination, with its own restrictions such as a less controlled environment, a continuous changing sun angle, (partly) cloud cover or ground reflections. These uncontrollable environmental parameters need to be taken into consideration as discussed in the methodology section below.

The challenges to be addressed are shown schematically in Fig. 1 and include: (i) the problem of air-filled bubble generation with a narrow diameter distribution, a key requirement for the GPPT approach; (ii) the development of the optical transfer function at different reproduction scales, which limits the use of the GPPT at larger volumes; (iii) the issue of a moving camera that requires continuous calibration; and (iv) the assessment of the overall flow reconstruction to be extracted with this novel technique. A well-documented canonical test case consisting of a turbulent free jet emanating from a square nozzle, with edge dimension of $l = 300$ mm, and a uniform outlet velocity of $U_e = 10$ m/s, is used to highlight both achievements and limitations in the context of the aforementioned study challenges.

2 Experimental methodology

2.1 Glare-point particle tracking (GPPT)

The current section gives an overview of the physical principals that are needed in order to fully understand the glare-point particle tracking approach and the discussion on the

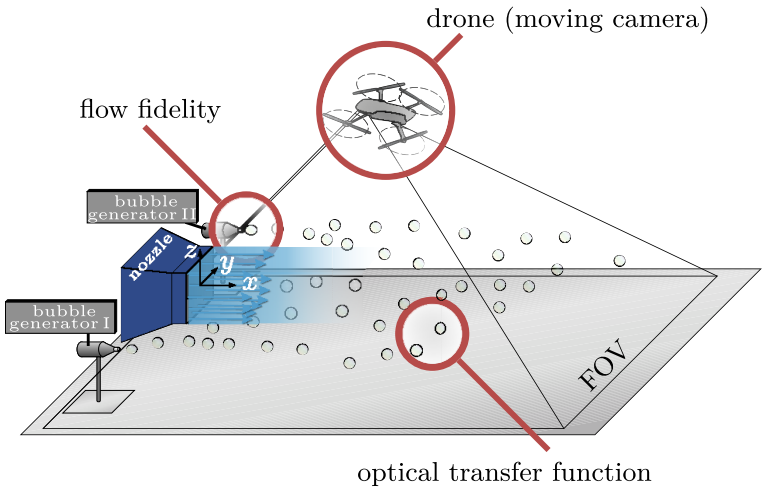

Fig. 1 Experimental setup highlighting challenges addressed in current study. A turbulent jet exits from the nozzle, and the subsequent flow is fed with AFSBs via two generators placed on either side of the nozzle. At the same time, the camera hovers above the field of view (FOV) at an approximate height of 7.8 m

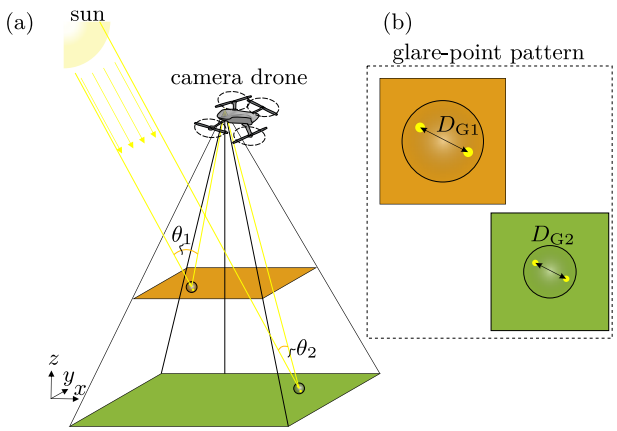

Fig. 2 Experimental setup with: **a** clarification of the trigonometric interrelations between the sun as light source, the bubbles and the camera drone; and **b** visualization of the glare-point pattern for the bubbles as they appear on the camera chip

limits and the applicable region later on. By using tracers with much larger diameters, the particle image on the camera chip shifts from a diffraction-based to geometrical imaging, where several glare points from the transparent soap bubble become visible. The first glare point can be associated with the direct reflection at the outer position of the soap film, whereas the second glare point represents the second reflection of the inner face of the soap bubble. Several additional glare points of higher orders can also be observed (but their light intensity is generally an order of magnitude lower). For the present approach, the distance of the two brightest glare points (first and second reflection) is used for depth extraction; see sensitivity analysis presented in Kaiser and Rival (2023).

Figure 2 shows the physical working principle of the GPPT approach. The flow is seeded with equally sized soap bubbles, which are subsequently illuminated by the sun. The refracted light is imaged on the camera sensor located on the drone. The angle between the sun, the bubble and the camera is labeled as θ. The angle depends on the position of the light source, since parallel rays from the sun can be assumed, and the position within the measurement volume. The distance between the two brightest glare points is merely a function of the angle θ and the diameter of the bubble D_B, and follows the relation

$$D_G = D_B \sin(\theta(x, y)/2). \tag{1}$$

Since the bubble diameter D_B is held constant for all bubbles, the glare-point distance D_G depends only on the angle θ, which is a function of x, y and the distance to the camera, i.e., the reproduction scale s^{xy}. A detailed step-by-step explanation is given in Section 2.3.

The imaging characteristic of the tracers by illumination strongly depends on the size of the tracers and the reproduction scale. While small aerosol-based droplets can be modeled with help of Mie-scattering via an illumination intensity model and diffraction-based imaging of the particle image on the sensor, larger tracers such as HFSBs and AFSBs are generally modeled with the help of geometric imaging. Equation 2 states the diameter dependence of a particle image d_p as it appears on the sensor with both terms from geometric and diffraction-based imaging while neglecting out-of-focus effects, as discussed in Olsen and Adrian (2000):

$$d_i^2 = \underbrace{M^2 \, d_p^2}_{\text{geometric image}} + \underbrace{5.95(M+1)^2 \lambda^2 f_\#^2}_{\text{diffraction}}. \tag{2}$$

The first term describes the geometric image with magnification M. The second term exists due to the diffraction of light on the aperture of the camera, where λ is the wavelength of the light and $f_\#$ the focal number of the lens. The factor

of 5.95 arises from the first minimum of the Bessel function (of the first kind), which is used to model the intensity of the diffraction itself. Note that for the glare points, each one is either considered separately—while geometric imaging applies—or in combination, when the points are much closer together that they appear as one intensity spot on the sensor. This effect limits the GPPT approach toward larger distances/heights, as discussed later on.

2.2 Bubble generation and flow fidelity

While aerosol-based droplets, e.g., di-ethyl-hexyl-sebacate (DEHS) or water–glycol particles, with a typical diameter in the range of $0.3 - 0.4$ µm (Fuchs et al. 2023), are suitable for small-scale measurements, larger particles with adequate particle image intensities need to be employed when moving to much larger scales. Typically helium-filled soap bubbles are used as tracer particles in air since their net buoyancy can be adjusted to perfectly follow the flow. Assuming a gravitationally induced velocity U_g from the Stokes drag law, this yields (following Raffel et al. 2018):

$$U_g = {d_p}^2 \frac{(\rho_p - \rho)}{18\mu} g, \tag{3}$$

where d_p is the particle diameter, ρ and ρ_p are the fluid and particle density, respectively, and μ is the dynamic viscosity of the fluid. Figure 3 shows the visualization of Eq. (3) for different particle sizes and densities, which results from different bubble wall thicknesses γ. Acceleration caused by gravitation or other sources are therefore captured properly at smaller particle diameters or with thin bubble wall thicknesses γ, whereas the assumption of Stokes flow breaks down once the relative slip velocity increases significantly. For low values of γ, the slip velocity remains comparatively small even for relatively large bubble diameters. Thus, a well-chosen bubble generation system where the bubble diameter as well as the amount of soap included in the film can be adjusted carefully is decisive for a meaningful fluid flow reconstruction.

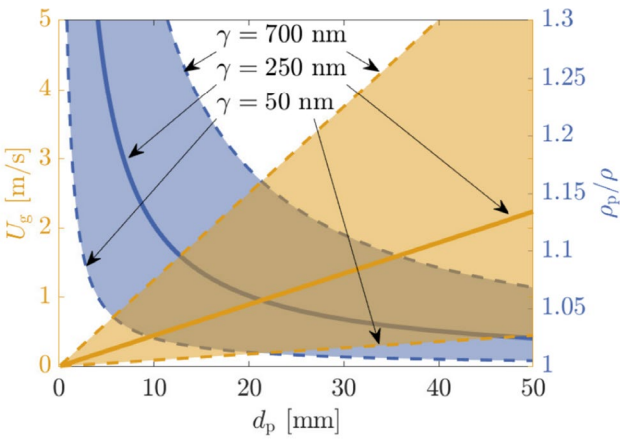

Fig. 3 Density ratio (ρ_p/ρ) and slip velocity (U_g) as a function of bubble diameter d_p. U_g is calculated assuming operation in the Stokes regime, where the drag law with Eq. (3) is valid. Values are visualized for a range of bubble wall thicknesses for $\gamma = 50$ nm to 700 nm. The density ratio decreases for larger particle sizes. The slip velocity, however, is shown to increase linearly with bubble diameter

The rationale behind a well-chosen bubble generation approach is twofold. The glare-point approach introduced by Hou et al. (2021) makes use of the glare-point distance to extract the third spatial coordinate (depth) of each bubble. Hence, a precise knowledge of the bubble diameter—ideally consistent for each individual bubble—is decisive. Hou et al. (2021) and Kaiser and Rival (2023) made use of a second camera for validation of the GPPT technique (i.e., to extract an error estimation during each of those initial experimental campaigns). The present study first explores the question of bubble diameter distribution beforehand via a small laboratory setup so as to avoid a second camera during the latter experiment with a drone. Findings from these initial laboratory-based tests are presented at the beginning of the "Results" section.

2.3 Experimental procedure

A large-scale (outdoor), canonical test case using a turbulent free jet with a square nozzle edge length of $l = 0.3$ m and an outlet velocity of $U_e = 10$ m/s was selected since this experiment serves as reliable baseline to explore the aforementioned study challenges. Two identical bubble generators producing AFSBs with mean diameters of 23.1 mm were used. Mean bubble diameters were verified in prior laboratory experiments with a double-illumination setup and a high-speed camera (Phantom SA4 equipped with a 50 mm Zeiss macro-planar lens, shutter speed and frame rate of 1/2000 s). The generators are placed at the symmetry plane of the nozzle in the horizontal z-direction at $x = 0$ and were pointed in the positive x-direction. The AFSBs initially experienced a strong acceleration within the entrainment region of the jet near-field, up to the end of the potential core. At this point, the bubbles were observed to reach the velocity of the jet itself, which was set to an exit velocity of 10 m/s. The jet Reynolds number, based on edge length, was approximately $U_e l/\nu$=166,000. Figure 4 shows an artificially multi-exposed raw data image for an overview of the test-up in the vicinity of the jet exit. The entire field of view (FOV) spans a maximum extent of $5.94 \times 10.56\,\mathrm{m}^2$. The pyramid-shaped measurement volume of the camera covers $V = (1/3)\ 5.94\,\mathrm{m} \times 10.56\,\mathrm{m} \times 7.8\,\mathrm{m} = 163\,\mathrm{m}^3$, where the factor 1/3 comes from the pyramidal shape of the measurement volume. The height of 7.8 m was chosen to fit the entire region of interest and additionally to avoid an influence to

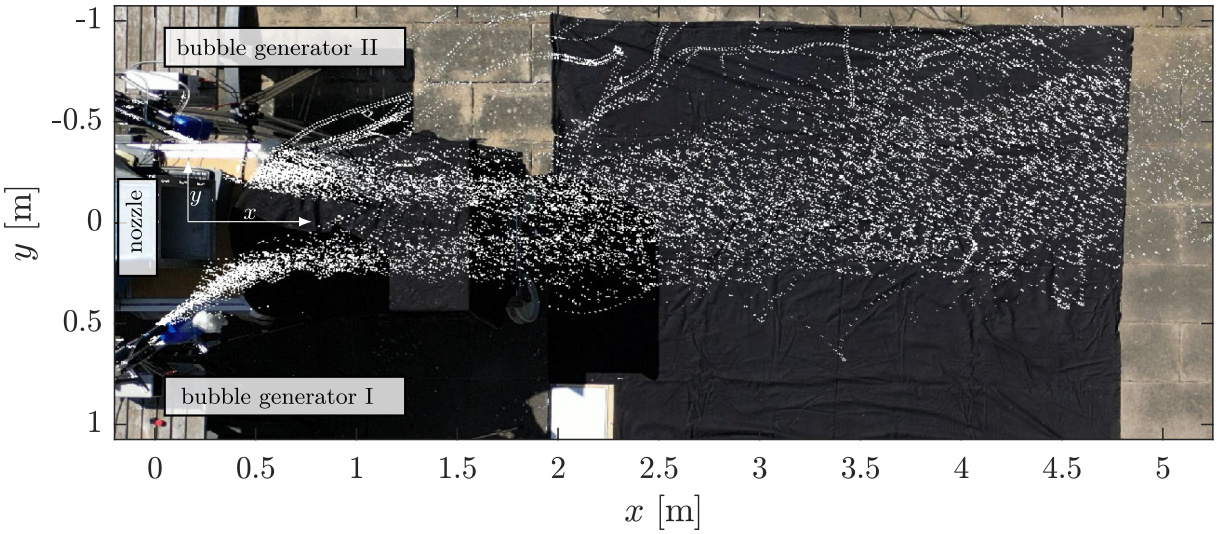

Fig. 4 Multi-exposed raw data image—section of the entire FOV—with 100 time steps of bubble movement. The jet nozzle and the bubble generators are visible on the left-hand side. The origin of the coordinate system $\{x, y, z\}$ is set to the nozzle exit

the drone's own flow. Preliminary tests of the rotor down wash state a negligible impact at this height to the flow on the ground. For the current experiment, a sequence of 25,359 frames were recorded, which leads to an effective time span of 7.04 min.

2.3.1 Camera setup, particle image and calibration

For the present study, measurements using an off-the-shelf, rotary-wing drone *DJI Mini 3 pro* with a takeoff weight of 249 g were carried out. The drone camera was equipped with an $1/1.3''$ CMOS sensor. The sensor features an overall resolution of 8064×6048 px, where a 4k resolution (3840×2160 px) was available within video mode at a frame repetition rate of max. 60 fps with a video bit rate of 150 Mbps, and a chosen shutter speed of $1/2000$ s to avoid motion blur. The pixel size is 2.4 µm (DJI-data sheet 2024), using so-called *quad Bayer coding*, where four pixels are combined. Within video mode, almost the entire width of the sensor is used; however, the image height is cropped to fit the commonly used 16-by-9 ratio. The effective binned pixel size in video mode was therefore 6.72 µm. According to the manufacturer, the lens is equipped with a 24 mm equivalent focal length with a fixed aperture of *f*/1.7. Since the camera setup is fixed, a simple calibration procedure was conducted, as explained later. The integral time scale of the flow can be estimated with the exit velocity U_e and the half of the exit diameter l and can be stated as $\tau_m = 0.5l/U_e = 0.015$ s, which fits to the frame rate of $1/60$ s. Based on this jet scale and camera operation limit, the integral quantities of the turbulent flow could be extracted.

According to Eq. (1), the distance of the glare points D_G is a function of the bubble diameter D_B and the angle θ between the sun and the camera. Figure 5 facilitates the process with help of a flow diagram and all relevant parameters. For the determination of θ, the elevation angle α of the sun needs to be known. The experimental test campaign took place on May, 8, 2024, at the inner courtyard of the ISM building at TU Braunschweig (52° 18' 50.122" N, 10° 32' 42.261" E).

The evaluated video started at 14:35 (UTC+2). The solar elevation angle α varies in this time period from 51.53° - 50.99°, compared to the horizon (NOAA-Calculator 2024). The camera was turned down to $\beta = -90°$ for a parallelization of the focus layer and the ground. The focus was set to the ground and manual focus was activated, such that no undesired refocusing occurs during the measurement. With the solar elevation angle, the direction of the camera and the position of the bubble within the raw image, the angle between the camera and the sun, which is called θ, can be calculated.

The next quantity to determine is the glare-point distance D_G with help of Eq. (1). This value is given in physical dimensions (e.g., mm) and compared with the pixel value of the extracted distance from the processed image data. This yields to one value of the image reproduction scale s^{xy} in mm/px for each bubble. The calibration function shown in Fig. 7b is used to extract the distance to the camera. With the calculated height of the drone, where an image-based approach was used as explained in Sec. 3.1, the height of each bubble with respect to the ground was determined.

Figure 7a shows an inverted raw data image with several bubbles at different distances to the camera and hence for

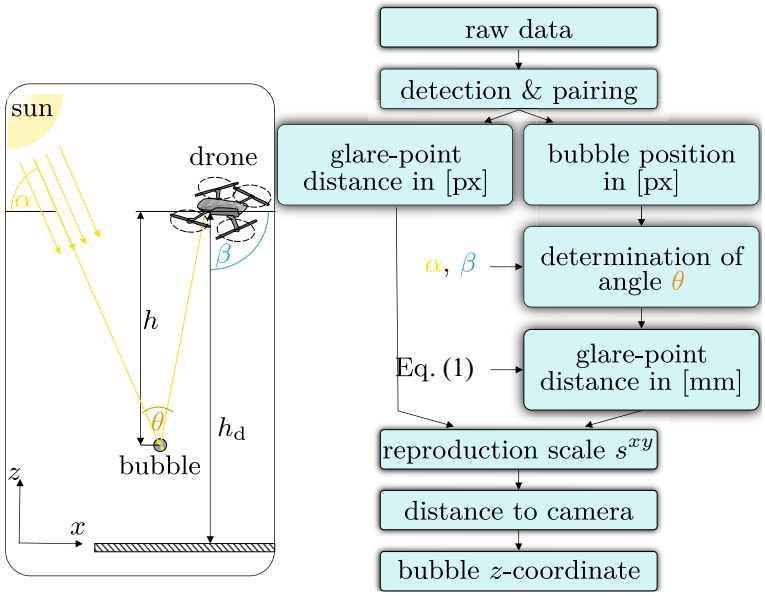

Fig. 5 Calculation and processing procedure with all relevant angles that were used for the GPPT technique

different magnifications. For bubbles imaged with a higher magnification, the outer edge is visible. All bubbles feature unifying characteristic glare points as dominant detection attributes. The number of glare points, however, changes due to for instance reflections from nearby the glass walls as well as the illumination angle. The focal layer was set close to infinity; consequently the bubbles closer to the lens experience some out-of-focus behavior, which is visible in the formation of polygonal glare points. Caused by the RGB sensor on the drone camera, different hue intensities become visible, which are a function of the (local) bubble wall thickness γ. The glare-point distances in this example are located between $7-120$ px, which correspond to a distance from the camera of $0.5-8.8$ m for the given experimental setup. Hence, for the magnification and camera setup provided by the *DJI Mini 3 pro*, the limit in height can be determined when the two most dominant glare points collapse onto one. This limit occurred well above 10 m in the present setup, which enables a theoretical investigation volume of up to 200 m^3. Figure 6 shows this limit for the given reproduction scale as a function of the angle θ as well as the height h for two theoretical detection limits between the glare points of 2 px and 4 px, and for three different bubble sizes (10, 23.1, 30 mm).

The results of the calibration procedure are shown in Fig. 7b. Caused by the fixed camera setup within the drone, no extensive multi-point calibration procedure needed to be performed during the experiments. Instead the calibration could be shifted to a controlled laboratory experiment in advance, where all distances could be identified with higher precision. A laser distance measurement device (*BOSCH Professional GLM 20*) was used to gain the distance from the lens to objects with a known vertical

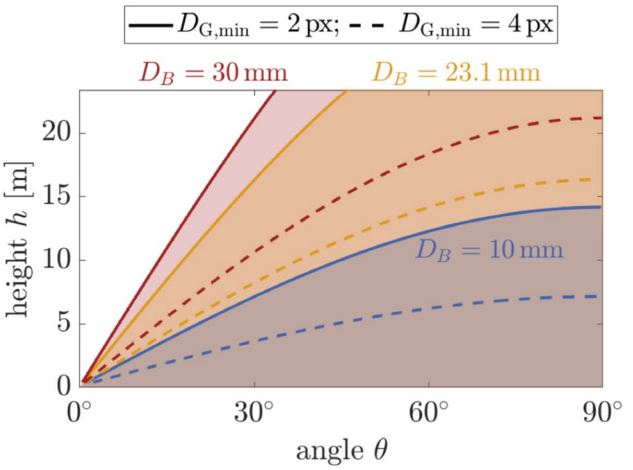

Fig. 6 The region, as well as limits, where two glare points are visible as a function of the angle θ and the height h, for three different bubble sizes (10 mm, 23.1 mm, 30 mm) and for two minimum distances (2 px and 4 px). The height is calculated using the image reproduction scale derived in Figure 7b

and/or horizontal extent parallel to the focus layer, which was set to infinity. It is important to mention that no so-called *focus breathing* was recognized, such that, despite the actual focus layer position, the obtained reproduction scales were valid throughout all possible focus configurations. Figure 7b shows the fitted linear slope that was used for the interrelation between the glare-point distance and the distance in space from the bubble to the camera. After the calibration procedure was complete, only a one-point calibration was necessary during the actual experiments, where a known geometrical pattern on the ground was used to validate the camera orientation parallel to the

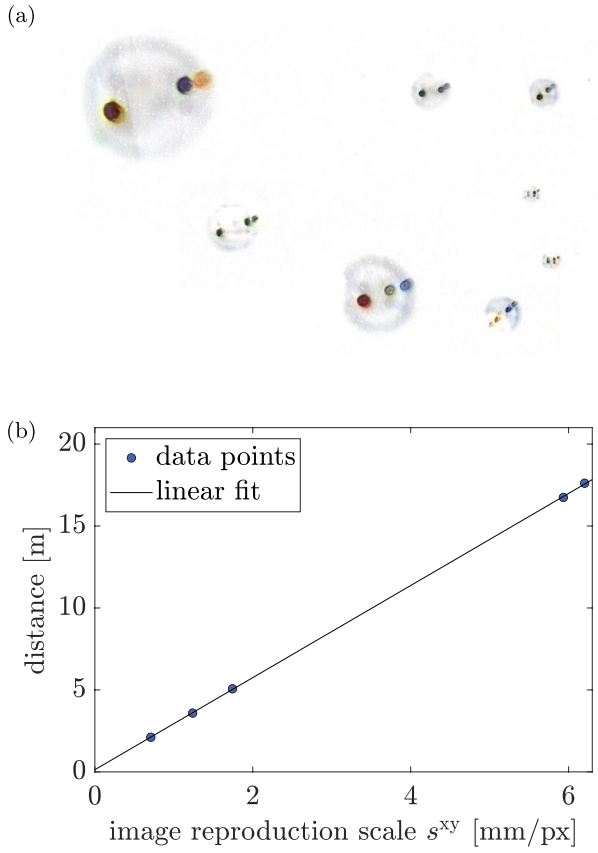

Fig. 7 **a** Brightness-inverted raw data image with background subtraction for several bubbles ranging from around 0.5 m up to 8.8 m distance. **b** Diagram of the reproduction scale s^{xy} at different object–lens distances as well as the interrelation for the glare-point approach

ground/horizon. This approach was necessary to quantify the movement of the camera/drone (as shown in the next section) and to double-check the glare-point distances with a known reproduction scale at a specific distance.

2.4 Post-processing procedure

The extracted videos were loaded into MATLAB 2022b (MathWorks, Inc.). Camera motion in x, y, z-direction was evaluated with the colored raw data images without any further processing. A cross-correlation of the exit nozzle provides the lateral movement, while a continuous detection of the edges of one rectangular flagstone from the ground serves as determination of the horizontal movement.

For the extraction of the particle tracks, a minimum filter—with respect to each color channel—with the two neighboring frames was applied to reduce the background information. The small number of frames considered for this operation is caused by the moving camera as otherwise objects on the stationary ground would appear within the background-subtracted image. The images were saved as monochromatic images and imported into DaVis 11 (LaVision GmbH) to proceed with the particle tracking procedure. The entire image extension was considered resulting in 25,359 black-and-white images with a resolution of 3840×2160 px. Within DaVis, a 2D particle tracking process with an intensity threshold of 25 intensity counts was applied. The results were reloaded into MATLAB for the calculation of the accelerations and the visualization of the entire Lagrangian tracks. The calculation of the glare-point distances was also calculated with MATLAB, since the particle tracks extracted from DaVis had several frames where only one of two glare points could be detected. For this reason, tracks were observed to be shorter after the three-dimensional reconstruction. The procedure described in Hou et al. (2021), where broken tracks could be repaired with help of the neighboring frames, works only for a sparse seeding density and thus could not be applied for the given experimental campaign.

3 Results

Prior to outdoor measurements, a small double-illumination setup, which combines backward illumination to account for the outer edge of the bubble and forward illumination for glare-point visibility, was used to quantify the relationship between the change of glare-point distances shortly after bubble generation. This method follows the approach in Kaiser and Rival (2023) where the spherical shape of the bubble could be detected by the outer edge in both x- and y-direction.

Figure 8a shows the glare-point distance as well as the outer shapes for one bubble closely after generation. All considered values initially fluctuate in time due to the bubble formation in the first instances after leaving the bubble generator. While the x and y values oscillate partly in an asynchronous manner, they rapidly reduce in magnitude at around 200ms due to a dampening via surface tension. The oscillation of the glare-point distance is still observable at 300 ms, when the bubble leaves the FOV. This observation is useful for the GPPT approach since any deviation from the ideal spherical shape of the tracer is therefore distinguishable by the change of the glare-point distance in time. The tracer itself can therefore call attention to any imperfect flow-following behavior by a quantity that is visible not only during these laboratory tests, but also during the latter outdoor experiments. Regions of the flow where the glare-point distances fluctuate in time can thus be considered with particular caution and eventually filtered out.

For the generation of equally sized bubbles, a 3D printed bubble generator was manufactured similar to the one used in Kaiser and Rival (2023). Figure 8c shows the

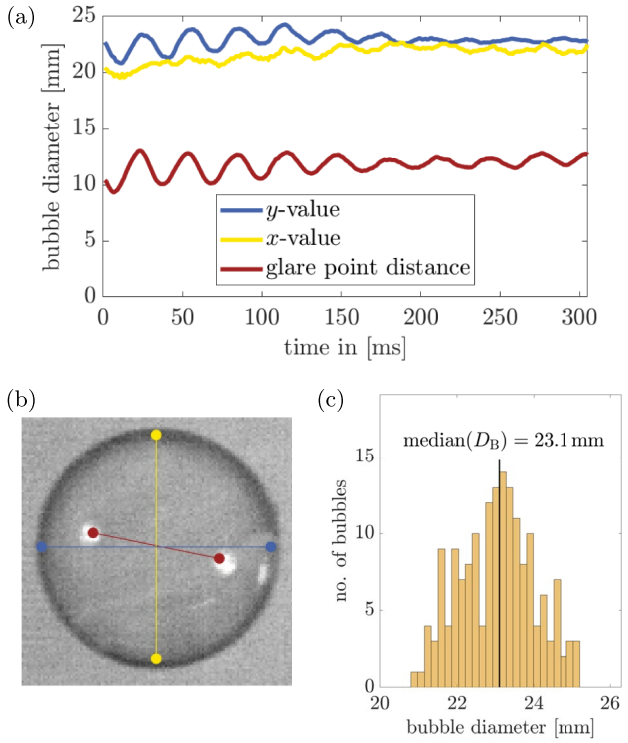

Fig. 8 **a** Horizontal, vertical and glare-point distance over time for one bubble. **b** Raw data of one bubble with indication of the horizontal edge (• *y*−values), the vertical edge (• *x*-values) and the glare-point distance (•). **c** Diameter distribution of the emerging bubbles close to the generator. The median of 23.1 mm is used for further processing

corresponding diameter distribution of the generated soap bubbles for one operational point.

3.1 Moving camera and depth quantification

Although the drone was positioned using the hover mode, it actively compensated due to slight local flow perturbations. Figure 9 shows the lateral and horizontal changes in position for a time span of 3600 frames (or one minute). The changes are depicted as pixel values on the left ordinate and the corresponding changes in physical coordinates are depicted with the right ordinate. The frame-to-frame displacement never reached values above one pixel. The summarized values are highest for the *y*-direction with a value of 15 px or 40 mm. Since a variation in all directions can be tracked, a consideration within post-processing is possible. When smaller time spans are considered, the obtained positional error might even be negligible. However, the active compensation by the drone is not designed to reach the initial FOV of the first frame. Thus, for longer recordings it was necessary to check whether the later FOV was consistent with the initial FOV.

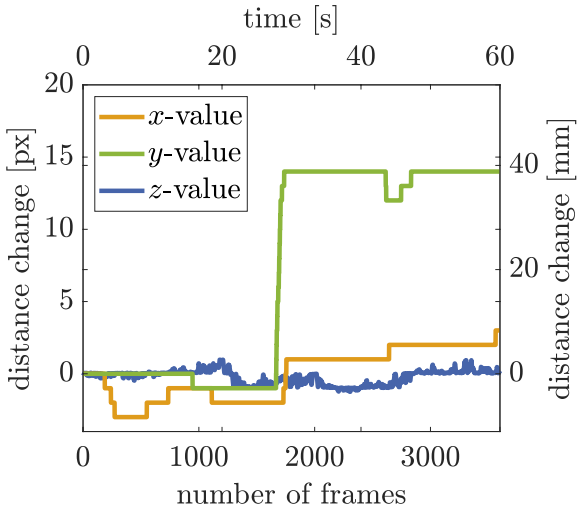

Fig. 9 Lateral (*x*, *y*) and horizontal (*z*) movement extracted from the image-based analysis

The said motion was obtained using an image-based approach, where each raw data image was compared to the next. Additionally, the frame-to-frame displacement could be tracked using the geo coordinates; for each frame, the camera states its horizontal and vertical position according to the geo-positioning coordinates and the internally built inertial measurement unit in a separate auxiliary file.

This estimation is, however, much coarser with a frame-to-frame variability of 0.1 m. The image-based displacement tracking is the favorable option for the present case due to its preciseness. With this information, the compensation mechanisms of the drone's internally built-in measurement unit could be quantified as well in all three dimensions.

Figure 10 shows 20 randomly chosen three-dimensional particle tracks. Since no second camera was used

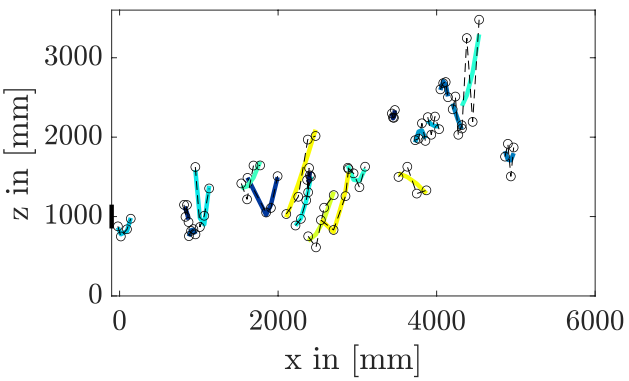

Fig. 10 Flow tracks with a length of four are shown in the *x*-*z* plane. The dashed lines show the linear connection between the detected bubbles, while the colored curves indicate a polynomial fit of second order. These quantities are used for the error quantification. The color indicates the velocity, and the color bar of Fig. 11 can be applied

for direct estimation of the measurement uncertainty, a quantification estimation was conducted via a polynomial fitting. The following assumption is made: The motion in both the z- and y-directions can be described by a second-order polynomial. Since the goal is to quantify the error in each spatial direction independently, the polynomial fitting is performed separately for the z- and y-components. All tracks with a track length of four were fitted with a polynomial fit of second order in z- and y-directions separately. The median value of the deviation between the actual position and the fitted position for each position yields a value of $\overline{\Delta y} = 0.28\,\text{mm}$ and $\overline{\Delta z} = 106.6\,\text{mm}$. The z-direction is thus more inaccurate, since this information is gained via the glare-point distance. With an uncertainty of 4.6 times, the bubble diameter this is for such a field experiment an acceptable tolerance and still enables the expression of values around the integral length scale of the jet, which was stated at $0.5\,l = 150\,\text{mm}$ Given the measurement depth of $h = 7.8\,\text{m}$, this yields a relative uncertainty of $\overline{\Delta z}/h = 1.37\%$.

3.2 Flow information

A large-scale turbulent free jet was studied, which inherently serves as challenging test case with strong accelerations and a broad range of scales. For this problem, the drone hovered at a height of approximately 7.8 m, which enabled a FOV of $5.94 \times 10.56\,\text{m}^2$, and hence a theoretical measurement volume of $163\,\text{m}^3$. This leads to a distance of 35 l (l being the characteristic length taken from the jet exit). The camera was directed parallel to the ground, and bubbles were supplied from two bubble generators placed close to the nozzle at the center of the nozzle in horizontal direction, pointing toward positive x-values, as

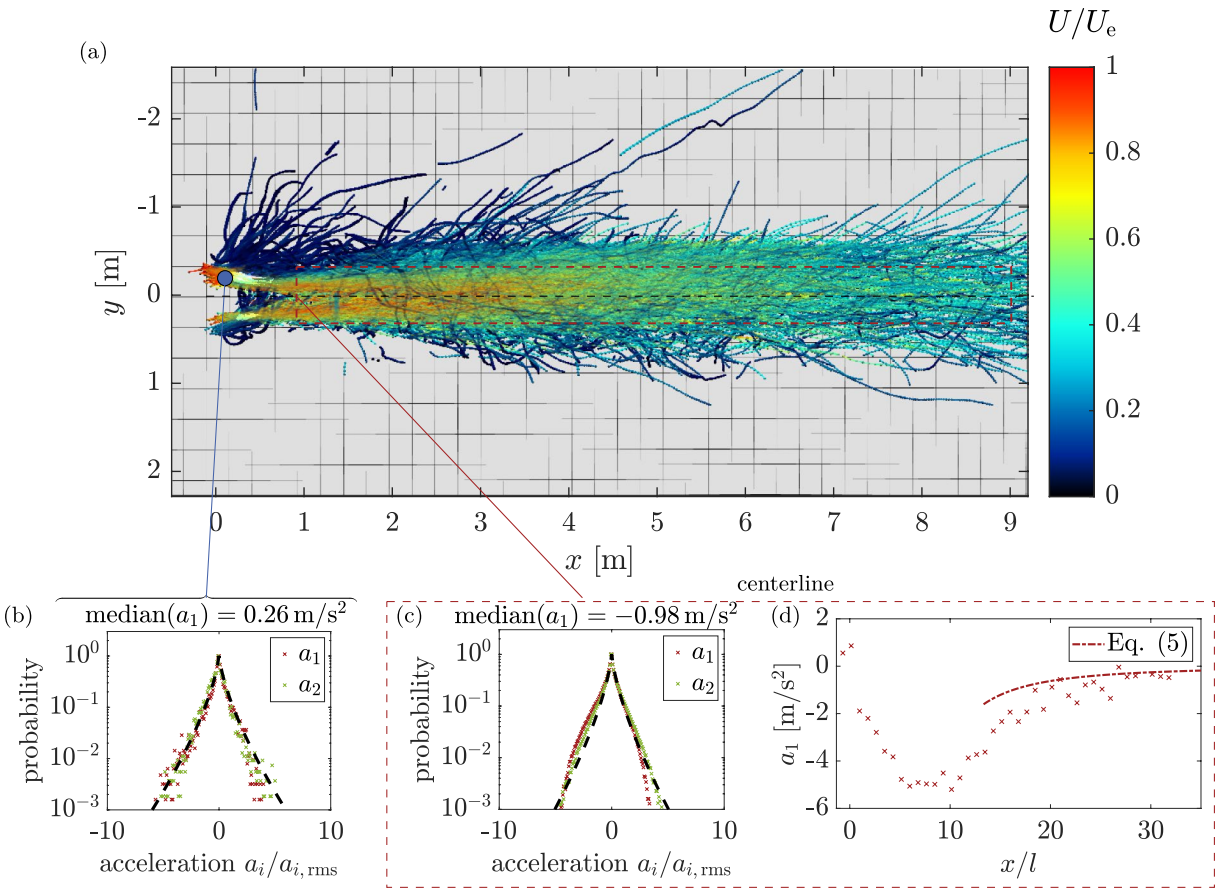

Fig. 11 Visualization of Lagrangian tracks for 1,000 time steps with color-coded normalized velocity. The exit velocity of the jet is $U_e = 10$ m/s. **b** Probability density distribution of the acceleration close to the generator, where a positive acceleration is present due to the entrainment in the jet. Dashed line follows the parametrization of La Porta et al. (2001) (Eq. 6) with $\beta_1 = 0.54$, $\gamma_1 = 1.3$ and $\sigma = 0.5$. ($a_{1,\text{rms}} = 22\,\text{m/s}^2$, $a_{2,\text{rms}} = 23\,\text{m/s}^2$) **c** Probability density distribution of the acceleration along the centerline with the same parametrization as in 11b ($a_{1,\text{rms}} = 26\,\text{m/s}^2$, $a_{2,\text{rms}} = 24\,\text{m/s}^2$). **d** Axial acceleration along the centerline, where the red dash dotted line represents Eq. 5)

visible in Figure 4. The bubbles were entrained into the flow following a strong acceleration followed by a continuous deceleration as part of the free jet system. Figure 11a shows all extracted tracks for 1,000 time steps from the particle tracking procedure conducted using DaVis 11. Due to overlapping particle tracks, and the need of partially transparent connecting lines, the visualization of DaVis was used directly. Note that color indicates the normalized velocity. The origin of the bubble generators is visible at $x = 0$. Figure 11b shows the acceleration distribution close to the upper generator. This is the only region where a positive mean acceleration in the x-direction occurs, conditioned by the entrainment of bubbles into the flow. Maximum acceleration values of $130\,\mathrm{m/s^2}$ could be detected. The acceleration distribution can be depicted with the help of Eq. (6). All other regions in the volume show a continuous deceleration, as is consistent with free jet theory. The acceleration distribution along the centerline is visible in Figure 11c, where the a_1-values (red crosses, ×) clearly deviate from the symmetric reference, a few cases at high positive values and a higher probability between $a_1/a_{1,\mathrm{rms}} = -5$ and -2. Figure 11d shows the acceleration along the normalized x/l-coordinate along the centerline. The positive values, where the bubbles accelerate at $x/l = 0$, could be extracted along with a constant deceleration at $5 < x/l < 11$ (with a minimum value of $-5.2\,\mathrm{m/s^2}$). This region is followed by a continuous asymptotic increase up to a value of 0. As reference, the red dashed line shows the interrelation of Eq. (5), which is only strictly valid in the self-similar region at values $x/l > 30$.

Turbulent jets are ubiquitous and hence are canonical in fluid-dynamics research. The flow conditions close to the outlet (low x/l-values) depend strongly on the exit geometry and the influence of the surroundings (in this so-called developing region, up to $x/l \approx 30$). After this point, the jet reaches self-similarity, which enables the prediction of statistical properties. The centerline velocity U_0, as well as its derivative along the main axis, can be extracted according to Pope (2000) via

$$\frac{U_0}{U_e} = \frac{B}{\frac{(x - x_0)}{d}}, \tag{4}$$

$$\frac{\mathrm{d}U_0}{\mathrm{d}x} = -\frac{U_0}{x}, \tag{5}$$

with B an empirical constant and x_0 defining the virtual origin. Eq. (5) is shown in Fig. 11d. In contrast, at a much smaller scale, Buchwald et al. (2024) applied dense STB-based Lagrangian particle tracking in the far-field of a round turbulent jet starting at x/l=90, where both acceleration and coherent flow structures could be obtained up to the Taylor microscale.

A useful parametrization of acceleration data in general was originally suggested by La Porta et al. (2001) in terms of an acceleration distribution parametrization in a fully developed turbulent flow and can be stated as

$$P(a) = C \exp \frac{-a^2}{((1 + |\frac{a\beta_1}{\sigma}|^{\gamma_1})\sigma_1{}^2)}, \tag{6}$$

with $\beta_1 = 0.539$, $\gamma_1 = 1.588$ and $\sigma_1 = 0.508$ being phenomenological constants for the flow under consideration. This equation, although only possible for use with a symmetric distribution, is included in Figure 11b and Figure 11c for comparison. We can observe strong agreement with our current very large-scale measurements, thus demonstrating the power in using a drone-based approach to obtain sparse yet nevertheless accurate acceleration fields.

Since the drone-based technique allows for sparse yet accurate particle tracks, further Lagrangian properties of the flow field can be evaluated. As suggested by Braun et al. (2006), intrinsic geometrical characteristics of space curves are suitable for a description of particles paths within turbulent flows. The curvature κ of a path can thus be calculated as

$$\kappa = \frac{1}{r_\mathrm{c}} = \frac{|\vec{u} \times \dot{\vec{u}}|}{|\vec{u}|^3}, \tag{7}$$

with r_c the curvature radius. This quantity is shown in Figure 12 for the centerline of the jet (cf. Figure 11) and two parallel lines at $y/d = \pm 2$. The maximum value of the centerline is reached at 0.77 m. The most frequent integral length scale along the jet axis is observed to be on the order of two times the jet exit diameter l. At the borders of the jet ($y/l = \pm 2$), this value is slightly smaller, reaching a maximum probability at 0.5 m, with an increased probability

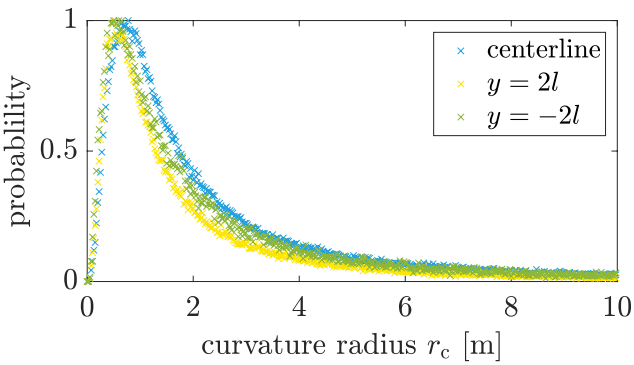

Fig. 12 Probability distribution of curvature radius r_c according to Eq. (7) for the centerline and peripheral region of the jet

between 0 m and 0.5 m, when compared to the centerline distribution.

4 Conclusions

In the current study, we assess the glare-point particle tracking (GPPT) technique in a complex field measurement scenario, where a drone-based, consumer-grade camera is used under natural light conditions. As tracer particles, large air-filled soap bubbles are used with a median diameter distribution on the order of 20 mm. In general, the use of a drone for imaging has been successful where the slight frame-by-frame movement during hover can be quantified by an image-based approach and in turn corrected for each individual frame. Furthermore, by continuously tracking the glare-point distance of each bubble in time we were able to identify (remove) specific tracks where extreme accelerations caused limitations in the flow-following behavior. It should also be noted that when in the future moving to larger volumes beyond 200 m^3, larger bubbles and/or a higher sensor resolution can eventually be employed. The subtle shifts of the camera could be avoided by using open-source autopilots and fixed-mount systems. The current setup enables a large variety of possible applications, from technical issues with real-sized models to suitable applications in industrial buildings, to profitable use in atmospheric flows.

It was also demonstrated that when eventually applying this new drone-based technique to large-scale facilities or complex terrain, the image calibration can successfully be completed beforehand. Finally, the exemplary test case of a large turbulent free jet demonstrates feasibility of the technique when moving to large field studies. The high-quality Lagrangian tracks, as well as their corresponding acceleration and curvature, can be extracted faithfully. Such data can provide insights into turbulent shear flows from a Lagrangian perspective where flow structures on the order of the integral length scale in the flow can be obtained. This data offers insights into turbulent shear flows from a Lagrangian viewpoint, enabling the capture of flow structures at scales comparable to the integral length and time scale.

Acknowledgements The authors would like to acknowledge the help of Dr. Michael Hilfer for his support and input during the experimental test campaign.

Author contributions R. Leister was responsible for data acquisition, data evaluation, writing—original draft and visualization, and D.E. Rival was responsible for data acquisition, writing—reviewing and editing, and project administration)

Funding Open Access funding enabled and organized by Projekt DEAL. We gratefully acknowledge the financial support for RL by the Karlsruhe House of Young Scientists (KHYS) at the Karlsruhe Institute of Technology (KIT) within the*KHYS Travel Grant, which enabled a research stay from May to September 2023 in Kingston, ON, Canada at Queen's University.*

Open-access funding was enabled and organized by *Projekt DEAL.*

Data availability Data are made available upon request.

Declarations

Conflict of interest The authors declare that they have no Conflict of interest.

Ethical approval not applicable

References

Barros DC, Duan Y, Troolin DR, Longmire EK (2021) Air-filled soap bubbles for volumetric velocity measurements. Exp Fluids. https://doi.org/10.1007/s00348-021-03134-6

Bosbach J, Kühn M, Wagner C (2008) Large scale particle image velocimetry with helium filled soap bubbles. Exp Fluids 46(3):539–547. https://doi.org/10.1007/s00348-008-0579-0

Bou-Zeid E, Anderson W, Katul GG, Mahrt L (2020) The persistent challenge of surface heterogeneity in boundary-layer meteorology: a review. Bound Layer Meteorol 177(2–3):227–245. https://doi.org/10.1007/s10546-020-00551-8

Braun W, De Lillo F, Eckhardt B (2006) Geometry of particle paths in turbulent flows. J Turbul 7:N62. https://doi.org/10.1080/14685240600860923

Bristow NR, Li J, Hartford P, Guala M, Hong J (2023) Imaging-based 3d particle tracking system for field characterization of particle dynamics in atmospheric flows. Exp Fluids. https://doi.org/10.1007/s00348-023-03619-6

Bristow NR, Pardoe N, Hong J (2023) Atmospheric aerosol diagnostics with UAV-based holographic imaging and computer vision. IEEE Robot Autom Lett 8(9):5616–5623. https://doi.org/10.1109/LRA.2023.3293991

Buchwald T, Schanz D, Godbersen P, Agocs J, Schröder A (2024) Large scale turbulent round free jet far field investigations using shake-the-box 3d lagrangian particle tracking. In: Proceedings of the 21st international symposium on application of laser and imaging techniques to fluid mechanics 2024, https://elib.dlr.de/205524/

Caridi GCA, Ragni D, Sciacchitano A, Scarano F (2016) HFSB-seeding for large-scale tomographic PIV in wind tunnels. Exp Fluids. https://doi.org/10.1007/s00348-016-2277-7

Conlin N, Even H, Wei NJ, Balantrapu NA, Hultmark M (2024) Lagrangian particle tracking in the atmospheric surface layer. Meas Sci Technol. https://doi.org/10.1088/1361-6501/ad56ac

Detert M, Weitbrecht V (2014) Helicopter-based surface piv experiments at thur river. In: Proceedings of the seventh international conference on river flow, Lausanne, Switzerland, https://doi.org/10.1201/b17133

Detert M, Weitbrecht V (2015) A low-cost airborne velocimetry system: proof of concept. J Hydraul Res 53(4):532–539. https://doi.org/10.1080/00221686.2015.1054322

Detert M, Cao L, Albayrak I (2019) Airborne image velocimetry measurements at the hydropower plant schiffmühle on limmat river, switzerland. In: Proceedings of the 2nd international symposium and exhibition on hydro-environment sensors and software, HydroSenSoft 2019, https://doi.org/10.3929/ethz-b-000341626

DJI-data sheet (2024) DJI Mini 3 Pro, User manual, V. 1.6. https://dl.djicdn.com/downloads/DJI_Mini_3_Pro/UM/20240105/2/DJI_Mini_3_Pro_User_Manual_v1.6_EN.pdf, last accessed on 2024-05-24

Faleiros DE, Tuinstra M, Sciacchitano A, Scarano F (2018) Helium-filled soap bubbles tracing fidelity in wall-bounded turbulence. Exp Fluids. https://doi.org/10.1007/s00348-018-2502-7

Fuchs T, Bross M, Kähler CJ (2023) Wall-shear-stress measurements using volumetric μptv. Exp Fluids. https://doi.org/10.1007/s00348-023-03656-1

Fujita I, Hino T (2003) Unseeded and seeded PIV measurements of river flows videotaped from a helicopter. J Vis 6:245–252. https://doi.org/10.1007/BF03181465

Grille Guerra A, Scarano F, Sciacchitano A (2024) On the scalability of helium-filled soap bubbles for volumetric PIV. Exp Fluids. https://doi.org/10.1007/s00348-024-03760-w

Hou J, Kaiser F, Sciacchitano A, Rival DE (2021) A novel single-camera approach to large-scale, three-dimensional particle tracking based on glare-point spacing. Exp Fluids. https://doi.org/10.1007/s00348-021-03178-8

Kaiser F, Rival DE (2023) Large-scale volumetric particle tracking using a single camera: analysis of the scalability and accuracy of glare-point particle tracking. Exp Fluids. https://doi.org/10.1007/s00348-023-03682-z

La Porta A, Voth GA, Crawford AM, Alexander J, Bodenschatz E (2001) Fluid particle accelerations in fully developed turbulence. Nature 409(6823):1017–1019. https://doi.org/10.1038/35059027

Li J, Guala M, Hong J (2024) Field investigation of 3-d snow settling dynamics under weak atmospheric turbulence. J Fluid Mech 997:A33. https://doi.org/10.1038/35059027

NOAA-Calculator (2024) Solar Calculator of the US National Oceanic & Atmospheric Administration (NOAA), Global Monitoring Laboratory. https://gml.noaa.gov/grad/solcalc/

Olsen MG, Adrian RJ (2000) Out-of-focus effects on particle image visibility and correlation in microscopic particle image velocimetry. Exp Fluids 29(7):S166–S174. https://doi.org/10.1007/s003480070018

Pope SB (2000) Turbulent flows. Cambridge University Press

Raffel M, Willert CE, Scarano F, Kähler CJ, Wereley S, Kompenhans J (2018) Particle image velocimetry, 3rd edn. Springer Berlin Heidelberg, Cham, https://doi.org/10.1007/978-3-319-68852-7

Rosi GA, Sherry M, Kinzel M, Rival DE (2014) Characterizing the lower log region of the atmospheric surface layer via large-scale particle tracking velocimetry. Exp Fluids. https://doi.org/10.1007/s00348-014-1736-2

Scarano F, Ghaemi S, Caridi GCA, Bosbach J, Dierksheide U, Sciacchitano A (2015) On the use of helium-filled soap bubbles for large-scale tomographic PIV in wind tunnel experiments. Exp Fluids. https://doi.org/10.1007/s00348-015-1909-7

Schröder A, Schanz D, Bosbach J, Novara M, Geisler R, Agocs J, Kohl A (2022) Large-scale volumetric flow studies on transport of aerosol particles using a breathing human model with and without face protections. Phys Fluids 10(1063/5):0086383

Wei NJ, Brownstein ID, Cardona JL, Howland MF, Dabiri JO (2021) Near-wake structure of full-scale vertical-axis wind turbines. J Fluid Mech 914:A17. https://doi.org/10.1017/jfm.2020.578